UNSTEADY HYDRODYNAMICS OF A BOX WHEN ENTERING A LOCK

Zhi-Ming Yuan, University of Strathclyde, UK
Yihan Liu, China Classification Society, CN
Momchil Terziev, University of Strathclyde, UK

UNSTEADY HYDRODYNAMICS OF A BOX WHEN ENTERING A LOCK

Yihan Liu, China Classification Society, CN
Momchil Terziev, University of Strathclyde, UK
Zhi-Ming Yuan, University of Strathclyde, UK

SUMMARY

The hydrodynamics of ships entering a lock are exceedingly complex. During this process, ships inevitably encounter a sudden narrowing of the channel and continuous or abrupt variations in water depth. The fluid is displaced and accelerates as it flows through the gaps between the ship, the lock walls, and the bottom, significantly increasing the risk of collision or grounding. As a result, the manoeuvrability of ships during lock entry has long been a topic of interest among researchers. However, beyond this focus, the intricate hydrodynamic phenomena associated with the free surface within the lock during ship entry have received relatively little attention. This paper aims to explore the causes of these phenomena and analyse their impacts on ship hydrodynamics, thereby providing further theoretical support for addressing manoeuvrability issues of ships during lock entry.

NOMENCLATURE

C_T	Total resistance coefficient
C_w	Wave making resistance coefficient
F	Force (N)
g	Density of water (kg/m^3)
L	Length (m)
B	Breadth (m)
D	Depth (m)
T	Draft (m)
P	Pressure (N/m^2)
R_w	Wave making resistance (N)
S	Area (m^2)
A_s	Cross section area (m^2)
t	Time (s)
U	Ship velocity (m/s)
v	Return flow velocity (m/s)
V	Volume(m^3)
ν	Kinematic viscosity (m^2/s)
ρ	Density of water (kg/m^3)
φ	Velocity potential
ζ	Velocity potential
δ	Blockage ratio
κ	Acceleration coefficient

1 INTRODUCTION

The dynamic behaviour of ships during lock entry remains an intricate and challenging topic, largely due to the complex interplay of hydrodynamic factors. Variations in channel design, depth changes, flow interactions, and the effects of confined spaces contribute to significant alterations in a ship's hydrodynamic environment. These changes are especially pronounced as vessels encounter restricted channel dimensions and reduced water depths when entering locks. The resulting compression of flow around the hull leads to increased velocity and reduced pressure, with potential consequences such as enhanced sinkage and trim. Additionally, differential pressure distributions can induce wave resistance and pitching moments, while lateral asymmetries in the waterway may cause unbalanced forces, raising the risk of unintended bank contact, grounding, or collision.

Real-world incidents, including the well-known Suez Canal blockage in 2021, highlight the operational challenges associated with navigating constrained waterways. To address these risks, significant research has been conducted on ship behaviour in confined settings. Investigations into shallow-water effects, bank proximity, and vessel interactions have been led by institutions such as the David Taylor Model Basin (1960), with experimental studies in locations like the Panama Canal. Other noteworthy contributions include analytical and experimental studies by Norrbin (1976) on bank effects, as well as model tests conducted by Flanders Hydraulics Research and Ghent University, exploring ship-bank (Lataire, et al., 2009; Lataire, et al., 2016), ship-bottom (Lataire, et al., 2012; Lataire, et al., 2016), ship-lock (Lataire, et al., 2012) and ship-to-ship interactions (Vantorre, et al., 2002). These efforts underscore the influence of boundary conditions on ship performance in narrow passages.

Wave phenomena associated with lock entry have also received some attention. Studies by Vrijburcht (1988) focused on calculating ship speeds and wave heights, while simulations by Meng and Wan (2016) analysed flow patterns during lock entry, highlighting water accumulation in front of the ship. More recent research by Wan et al. (2022) examined water-level fluctuations in specific lock configurations, linking these to operational parameters such as discharge rates and emptying sequences. Despite these contributions, there has been limited exploration of the wave fields generated as ships enter locks, particularly regarding their impact on hydrodynamic forces and ship responses.

This paper seeks to fill this gap by enhancing the capabilities of the potential flow solver MHydro, which employs a three-dimensional boundary element method with Rankine source functions. By refining the solver, this study aims to capture the unsteady wave phenomena occurring during lock entry and evaluate their implications for ship hydrodynamics in restricted waterways. The methodology is detailed in Section II, followed by an analysis of wave dynamics for simplified geometric cases in Section III. Key findings and their broader implications are discussed in Section IV.

2 MATHEMATICAL MODELLING

2.1 BOUNDARY VALUE PROBLEM

As depicted in Figure 1, this study employs two distinct right-hand coordinate systems: a global coordinate system *O–XYZ*, fixed to the midpoint of the lock entrance, and a local coordinate system o_0-$x_0y_0z_0$, positioned at the geometric center of the ship.

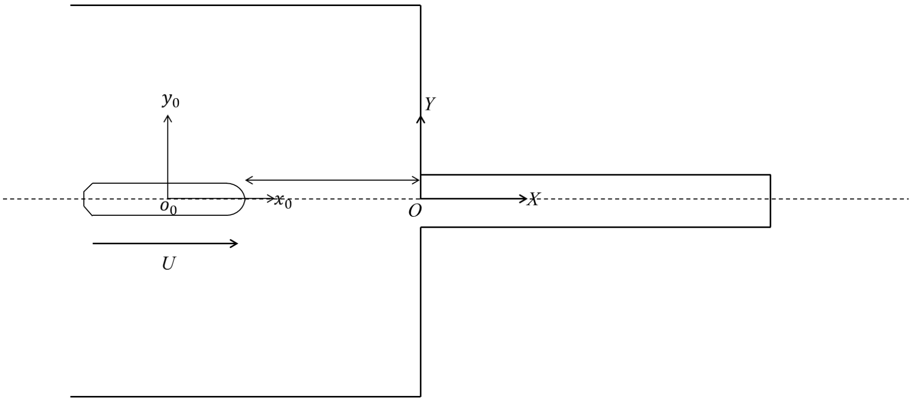

Figure 1 Sketch of the problem

In the global coordinate system, the *x*-axis points from the lock entrance toward the lock gate. Meanwhile, in the local coordinate system, the *x*-axis runs from the stern to the bow of the ship, with both *z*-axes pointing upward as the positive direction. The ship advances at a constant speed *U* along the positive *x*-axis while gradually entering the lock. This study assumes an ideal fluid based on potential flow theory, meaning the fluid is considered inviscid, irrotational, and incompressible. The flow is characterized by the velocity potential $\varphi(x, y, z, t)$ and the free surface is described by the wave elevation $\zeta(x, y, t)$.

The velocity potential $\varphi(x, y, z, t)$ satisfies the Laplace equation:

$$\frac{\partial^2\varphi}{\partial x^2}+\frac{\partial^2\varphi}{\partial y^2}+\frac{\partial^2\varphi}{\partial z^2}=0, \tag{1}$$

The free surface is expressed by the kinematics and dynamics free surface conditions,

$$\frac{\partial\zeta}{\partial t}-U\frac{\partial\zeta}{\partial x}+\frac{\partial\varphi}{\partial x}\frac{\partial\zeta}{\partial x}+\frac{\partial\varphi}{\partial y}\frac{\partial\zeta}{\partial y}-\frac{\partial\varphi}{\partial z}=0, at\ z=\zeta \tag{2}$$

$$\frac{\partial\varphi}{\partial t}-U\frac{\partial\varphi}{\partial x}+g\zeta+\frac{1}{2}\nabla\varphi\cdot\nabla\varphi+\frac{P}{\rho}=0, at\ z=\zeta \tag{3}$$

where φ_t and ζ_t are the time derivative of φ and ζ. φ_x, φ_y, and φ_z are the x, y, and z-direction derivatives of φ, respectively.

In this study, it is crucial to acknowledge that the omission of nonlinear terms in free surface conditions results in an inability to evaluate the impact of nonlinear effects on unsteady phenomena comprehensively. Nevertheless, by referencing established research, certain relevant conclusions can still be drawn. Specifically, when a ship undergoes prolonged acceleration in shallow water, its wave resistance can be effectively predicted using both the linear and unsteady potential flow solver, MHydro, and computational fluid dynamics (CFD) methods. Importantly, predictions from these approaches align closely, with only slight discrepancies observed near critical speeds (Terziev, et al., 2024). This finding highlights the predominant role of unsteady effects in wave-making resistance at low speeds in shallow water, where the influence of nonlinear effects is comparatively minor.

Then, the free surface conditions are discretized by inducing and extending the numerical program MHydro (Yuan, 2019; Li, et al., 2020). Specifically, a kind of three-level scheme is used to obtain the derivatives of φ and ζ in the time and location scale,

$$(\varphi_{\mathrm{t}})_{\mathrm{i,j}}^{\mathrm{m+1}} = \frac{1}{\Delta t}\left(\frac{3}{2}\varphi_{\mathrm{i,j}}^{\mathrm{m+1}} - 2\varphi_{\mathrm{i,j}}^{\mathrm{m}} + \frac{1}{2}\varphi_{\mathrm{i,j}}^{\mathrm{m-1}}\right) \tag{4}$$

$$(\zeta_{\mathrm{t}})_{\mathrm{i,j}}^{\mathrm{m+1}} = \frac{1}{\Delta t}\left(\frac{3}{2}\zeta_{\mathrm{i,j}}^{\mathrm{m+1}} - 2\zeta_{\mathrm{i,j}}^{\mathrm{m}} + \frac{1}{2}\zeta_{\mathrm{i,j}}^{\mathrm{m-1}}\right) \tag{5}$$

$$(\varphi_{\mathrm{x}})_{\mathrm{i,j}}^{\mathrm{m+1}} = \frac{1}{\Delta x}\left(\frac{3}{2}\varphi_{\mathrm{i,j}}^{\mathrm{m+1}} - 2\varphi_{\mathrm{i,j+1}}^{\mathrm{m+1}} + \frac{1}{2}\varphi_{\mathrm{i,j+2}}^{\mathrm{m+1}}\right) \tag{6}$$

$$(\zeta_{\mathrm{x}})_{\mathrm{i,j}}^{\mathrm{m+1}} = \frac{1}{\Delta x}\left(\frac{3}{2}\zeta_{\mathrm{i,j}}^{\mathrm{m+1}} - 2\zeta_{\mathrm{i,j+1}}^{\mathrm{m+1}} + \frac{1}{2}\zeta_{\mathrm{i,j+2}}^{\mathrm{m+1}}\right) \tag{7}$$

where m represents the m^{th} time step and i and j indicate that the element is located on the i^{th} row and j^{th} column on the free surface. As a result, the kinematic free surface condition can be discretized first at iterative step k as

$$\frac{1}{\Delta t}\left(\frac{3}{2}\zeta_{\mathrm{i,j}}^{(\mathrm{m+1,k})} - 2\zeta_{\mathrm{i,j}}^{(\mathrm{m,k})} + \frac{1}{2}\zeta_{\mathrm{i,j}}^{(\mathrm{m-1,k})}\right) - \frac{U}{\Delta x}\left(\frac{3}{2}\zeta_{\mathrm{i,j}}^{(\mathrm{m+1,k})} - 2\zeta_{\mathrm{i,j+1}}^{(\mathrm{m+1,k})} + \frac{1}{2}\zeta_{\mathrm{i,j+2}}^{(\mathrm{m+1,k})}\right) - \frac{\partial\varphi_{\mathrm{i,j}}^{(\mathrm{m+1,k})}}{\partial z} = 0, \tag{8}$$

Then, the value of $\zeta_{\mathrm{i,j}}^{\mathrm{m+1}}$ is obtained accordingly, and updating the value of unknown potential φ at $t^{\mathrm{m+1}}$ also becomes feasible now,

$$\frac{1}{\Delta t}\left(\frac{3}{2}\varphi_{\mathrm{i,j}}^{(\mathrm{m+1,k})} - 2\varphi_{\mathrm{i,j}}^{(\mathrm{m,k})} + \frac{1}{2}\varphi_{\mathrm{i,j}}^{(\mathrm{m-1,k})}\right) - U\frac{\partial\varphi_{\mathrm{i,j}}^{(\mathrm{m+1,k})}}{\partial x} + g\zeta_{\mathrm{i,j}}^{(\mathrm{m+1,k})} = 0, \tag{9}$$

The calculation mentioned in above Eq. 8 and Eq. 9 pertains to the results obtained during the current k_{th} iteration. These results must undergo verification against pre-defined accuracy criteria $|\varphi_{\mathrm{i,j}}^{(\mathrm{m,k})} - |\varphi_{\mathrm{i,j}}^{(\mathrm{m,k-1})}| < \varepsilon$ and $|\zeta_{\mathrm{i,j}}^{(\mathrm{m,k})} - \zeta_{\mathrm{i,j}}^{(\mathrm{m,k-1})}| < \varepsilon$ where ε equals to 0.00001. Only when all specified conditions are satisfied can the computation proceed to the iteration of the next time step.

Apart from the free surface conditions, the boundary conditions on body should reflect the body surface is impenetrable and the value of the flow's normal velocity should be the same as the ship velocity U,

$$\frac{\partial\varphi}{\partial\boldsymbol{n}} = Un_1, \tag{10}$$

where $\boldsymbol{n}=(n_1, n_2, n_3)$ is the unit normal vector on body surface. On the sea bottom and side walls, the same boundary condition with the body surface is applied, but the normal velocity of flow here should equal to zero,

$$\frac{\partial\varphi}{\partial\boldsymbol{n}} = 0, \tag{11}$$

After the unknown velocity potential φ has been solved, the forces/moments can be obtained from the Bernoulli's equation,

$$F_{\mathrm{i}} = \iint_S Pn_{\mathrm{i}}dS, \qquad i = 1,2,\dots,6 \tag{12}$$

where i represents the degree of freedom, and

$$P = -\rho\left[\frac{\partial\varphi}{\partial t} - U\frac{\partial\varphi}{\partial x} + \frac{1}{2}(\nabla\varphi)^2\right], \tag{13}$$

Similarly, the free surface elevation can be expressed as

$$\zeta(x, y, t) = -\frac{1}{g}\left[\frac{\partial\varphi}{\partial t} - U\frac{\partial\varphi}{\partial x} + \frac{1}{2}(\nabla\varphi)^2\right], \tag{14}$$

2.2 RETURN FLOW COEFFICIENT

Although the box sails along the positive x-direction with a constant speed U, once it reaches the entrance of the lock, the water volume will increase due to the sudden narrowing of the waterway. This increase in volume elevates the free surface height within the lock and induces significant return flow inside the lock. This return flow has a substantial impact on the results. In the present study, the effect of return flow will be incorporated into the body surface boundary condition. The increased volume can be expressed as

$$\Delta V = UA_{\mathrm{s}}(t) \cdot \Delta t, \tag{15}$$

where A_{s} is the cross section area of the box's wetted surface at moment t. This means a return flow will follow and the same volume of water will flow through the clearance between the ship and the lock bank. As the box keeps entering the lock, the distance between the bow of the box and the lock gate will continue to decrease, which results in an increase in the return flow velocity $v(x, t)$ (Yuan, 2019). Considering the return flow as a uniform flow, the effect of the return flow can be treated as an additional time-dependent velocity term on body surface boundary condition $v(t)$,

$$\frac{\partial\varphi}{\partial n} = [U + v(t)]n_1, \tag{16}$$

where $v(t)$ can be obtained by

$$v(t) = \begin{cases} 0, & \text{while } t < t_{\mathrm{e}} \\ \kappa\frac{\delta}{l}(t - t_{\mathrm{e}})U^2, & \text{while } t_{\mathrm{e}} < t \le t_{\mathrm{c}} \end{cases} \tag{17}$$

where δ is the blockage ratio, which equals the ratio of the cross section area of the box to that of the lock, l is the lock length, t_{e} represents the moment when the box arrives at the entrance of the lock, and t_{c} represents the moment when the ship is totally in the lock.

As the existence of the return flow, the box will receive an acceleration and κ is the acceleration coefficient. After the moment t_{c}, the return flow will persist. Nevertheless, the acceleration coefficient will be reduced to a value smaller than κ. This is because, at this stage, the total water volume within the lock remains constant, and the return flow primarily results from variations in the displaced water volume. In this case, an empirical iteration method is introduced to estimate the return flow velocity,

$$v(t_{\mathrm{n}}) = v(t_{\mathrm{n-1}}) + \kappa\frac{\delta}{l}(U\Delta t)[v(t_{\mathrm{n-1}}) - v(t_{\mathrm{c}}) + U], \qquad \text{while } t > t_{\mathrm{c}} \tag{18}$$

where $v(t)$= $v(t_{\mathrm{c}})$ is the initial condition of Eq. 18.

2.3 NUMERICAL SIMULATION SETUP

In the numerical modelling process, panels are exclusively arranged on the body surface, free surface, and bank surface. To optimise computational efficiency, the bottom surface was not explicitly represented in the simulation. Instead, mirroring techniques were applied, treating the bottom surface as a reflective boundary to account for its effect on the computational outcomes. Likewise, this study utilises the symmetry of the computational domain, modelling only half of it.

Additionally, based on testing, the computational domain was truncated at a distance equivalent to four ship lengths aft of the stern. At this boundary, no influence on the simulation results was observed. Furthermore, as previously stated, the free surface remains continuous within the time domain, advancing alongside the ship. This ensures that the panels on the free surface maintain a constant distance from the ship's hull throughout the simulation.

The wave making resistance in this study has been non-dimensionalized and denoted as the wave making resistance coefficient,

$$C_{\mathrm{w}} = \frac{R_{\mathrm{w}}}{(1/2)\rho U^2 S}, \tag{19}$$

where S is the area of the wet body surface and R_{w} denotes the wave making resistance, which equals F_1 in Eq. 12.

A convergence analysis is also included in this study to ensure the stability of the numerical simulation results, as shown in Figure 2,

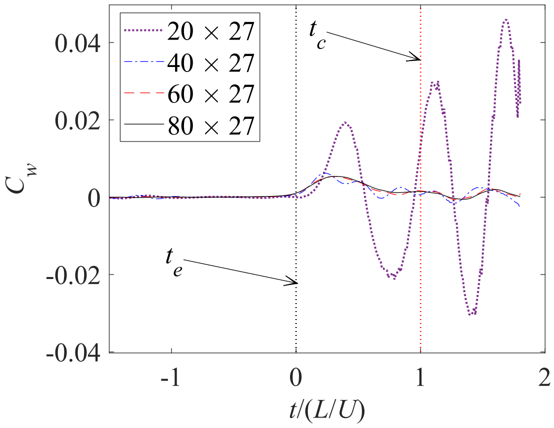

Figure 2 Convergence study on the numerical model, where C_{w} is the wave making resistance coefficient and $t/(L/U)$ is the dimensionless over time t.

The convergence study of the number of panels on the free surface includes four sets of grids, i.e., 40×27, 60×27, and 80×27 panels in the *x* and *y* directions within each ship length. It is observable that when the density of mesh is relatively sparse, the predicted wave making resistance exhibits considerable volatility, with the resistance curve not being smooth. However, as the density increases, these issues are noticeably ameliorated. After considering both the accuracy of the computational results and computational efficiency, this study uses the third set of grids to construct the numerical model.

Simultaneously, the fully unsteady approach adopted in this study necessitates that all results remain interconnected across each time step. This method imposes stringent requirements on the selection of the time step to ensure accuracy and stability. Consequently, the time step for this simulation was determined to be 0.0139s.

3 RESULTS AND DISCUSSION

This study delves into the hydrodynamic phenomena encountered by objects navigating through confined waterways. To ensure the research results align more closely with practical conditions, the study involves a box entering a lock at a low velocity within a confined channel. The selection of the dimensions for both the box and the lock will be explained later in this chapter

3.1 EXPERIMENTAL SETUP

The experiment was conducted in the towing tank of the Kelvin Hydrodynamics Laboratory (KHL), which boasts dimensions of 76 m in length, 4.6 m in width, and a maximum depth of 2.5 m, as illustrated in Figure 3. Further comprehensive details regarding this facility can be accessed via KHL's official website.

Figure 3 The towing tank of KHL.

The third set of lock chambers of the Panama Canal, which have a length varying between 427 and 488 m and a width of 55 m (Delefortrie, et al., 2009), was chosen as the lock model.

To simplify model construction and enable effective benchmarking against experimental data, this study selected a bulk carrier with a block coefficient (CB) close to 1. This choice facilitated the approximation of the ship's hull as a box-like structure for experimentation, with a scale model constructed at a 1:115 ratio. The detailed dimensions of the model box and the lock are provided in Table 1.

Table 1 Model Information.

	Lock(MS)	Box(MS)
L(m)	3.5	2.4
B(m)	0.5	0.4
T(m)	0.225	0.15
D(m)	0.3	0.2

In the test setup, water level fluctuations were monitored using wave gauges placed at five distinct locations, as illustrated in Fig. 19(c). An ultrasonic wave probe, moving synchronously with the box, recorded the wave elevations at the bow. Meanwhile, four fixed resistance wave gauges were used to measure the wave patterns within the lock.

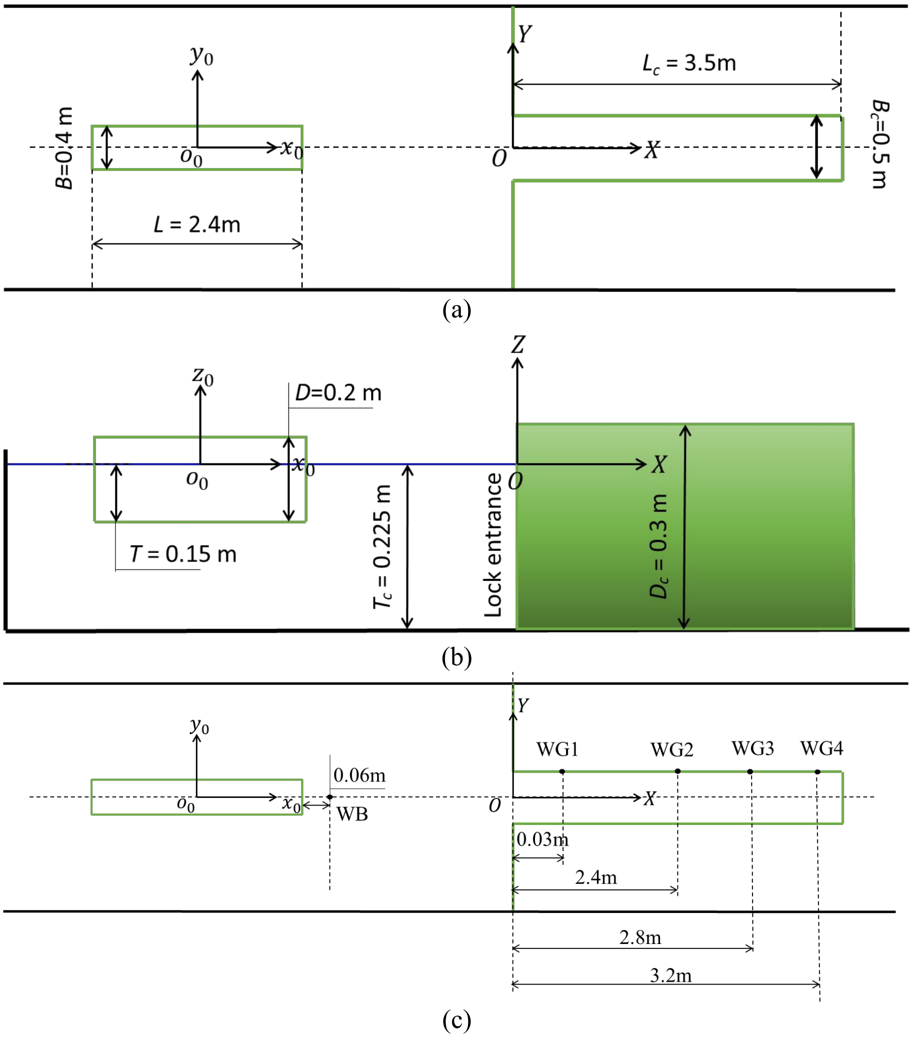

Figure 4 General layout of the towing tank for a box entering a lock and the positions of wave gauges: (a) top view of the tank; (b) side view of the tank; and (c) the positions of wave gauges.

In the experiments, marine plywood was used to construct both the ship and lock models. The ship model was carefully ballasted to ensure it remained watertight. To stabilise the lock model at its location, external L-shaped wooden supports were added, allowing weights to be applied for additional stability (refer to Figure 5). The box model was pulled by a carriage featuring a computer-controlled digital drive, offering precise and repeatable speed control. All six degrees of freedom of the box were constrained, meaning sinkage and trim were determined with the applied force divided by the hydrostatic restoring force. A Kistler piezoelectric multicomponent dynamometer was positioned at the connection between the box and the carriage to accurately measure the resistance encountered by the box during its lock entry process. This apparatus provided measurements of sway force and yawing moment around the box's origin.

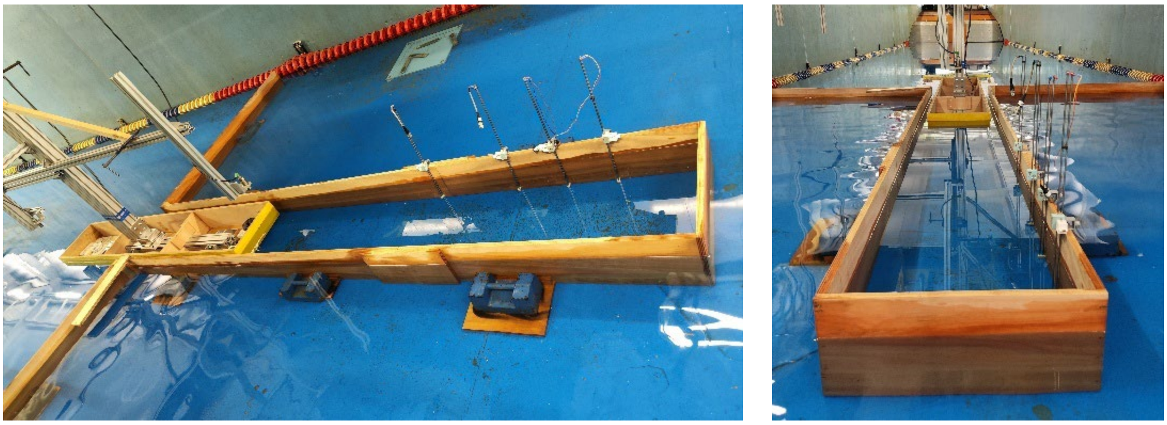

Figure 5 Floating box entering the lock.

Given the unsteady conditions of the tests, the reproducibility of the results is strongly influenced by the acceleration phase of the box and the abrupt narrowing of the channel. This effect is particularly pronounced when the box begins accelerating too close to the lock entrance, leading to noticeable disturbances in the measured wave heights inside the lock, especially near the entrance. To mitigate this issue, the tests were initiated in calm water, with the starting point of acceleration positioned 12 m away from the lock entrance. This arrangement ensures that the box has sufficient distance to reach its desired speed before approaching the entrance, thereby reducing the influence of acceleration-induced waves.

3.2 VALIDATIONS AND DISCUSSION OF THE NUMERICAL SIMULATION

The panel distribution of this case in the simulation is shown in Figure 6. It can be seen, the computational domain is truncated at 3.5*L* upstream, 1*L* sideways, and 3.5*L* downstream. This study ultimately arranged 520 panels on the body surface, 2746 panels distributed across the free surface, and 1510 panels on the bank surface.

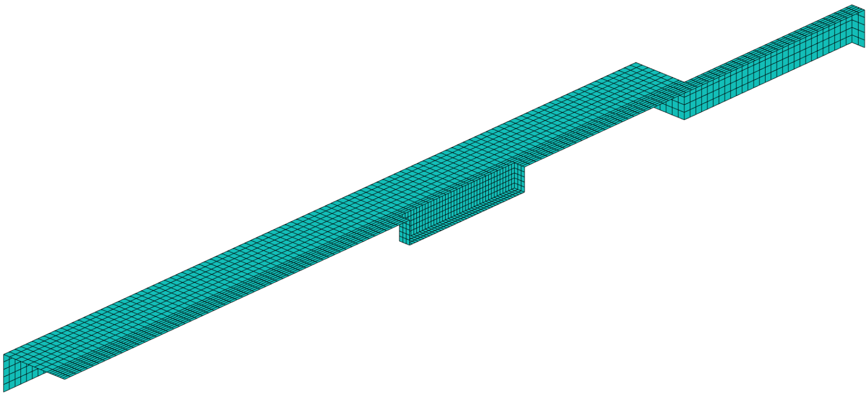

Figure 6 Panel distribution on the computation domain of a box entering a lock Model.

The experiment was conducted under five distinct velocity conditions, represented by U values of 0.1, 0.15, 0.2, 0.25, and 0.3 m/s. For comparative analysis, results from three experimental cases with velocities of $U = 0.1$ m/s ($Fr = 0.02$), $U = 0.2$ m/s ($Fr = 0.04$), and $U = 0.3$ m/s ($Fr = 0.06$) were specifically examined.

In addition to the experimental results, simulation results from CFD are also introduced in this paper to increase the confirmation of the reliability of the MHydro results. The CFD solutions are produced using the commercially available solver Star - CCM+. The developed model makes use of the Wilcox k - ω turbulence model with second order convective accuracy following previous experience, which indicates computational efficiency and accuracy with this model. The near-wall mesh is determined a priori using the approach detailed in with a $y^+ < 1$ in all cases. The free surface is resolved using the volume of fluid method, and since the time is discretized using a second order accurate scheme, the Courant number is limited to 0.5.

This determines the time step, which is set to ensure the Courant number is 0.3 to accommodate local flow acceleration. The body is encased in an overset mesh and translated in the x direction only. The results simultaneously include both pressure resistance and frictional resistance.

The computational boundaries are arranged to mirror the towing tank experiment as much as possible: the domain sides and bottom are no-slip walls. The domain top is placed one body length vertically from the undisturbed free surface, which is assigned a symmetry boundary condition, in addition to the plane coincident with the domain and body midplane. A pressure outlet boundary is placed approximately to match the experiment. The mesh on the free surface is progressively refined until 15 cells per transverse wavelength ($\lambda = 2\pi U^2 / g$) are achieved.

As shown in Figure 7, the total resistance experienced by the box exhibits a clear stepwise increase with rising velocity. This pattern is largely a result of unsteady effects. Higher velocities cause a larger volume of water to enter the lock within the same timeframe, intensifying the constriction effect of the channel. This, in turn, amplifies the unsteady behaviour.

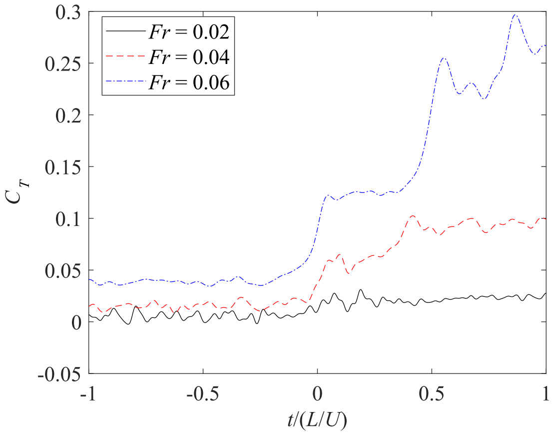

Figure 7 Results of the model experiments at different Froude numbers, where C_T is the dimensionless coefficient of the total resistance applied on the box: the x-axis represents both the dimensionless time and, simultaneously, the position of the bow of the box throughout the process of it entering the lock. When *t*/(*L*/*U*)= 0, the bow of the box has just reached the entrance of the lock.

Before commencing this study, it was observed that during a ship's entry into a lock, the water surface within the lock exhibited simultaneous rising and falling motion. This phenomenon was also replicated in model experiments involving an ellipsoid entering a lock (Liu, et al., 2024). In this paper, such movement of the free water surface is referred to as "piston motion." To ensure that the experimental results more closely align with real-world conditions, model experiments involving a box entering a lock were designed, as described in this study.

However, as illustrated in Figure 8, a comparison of the waves generated by the box within the lock at varying velocities reveals that the expected piston effect is barely noticeable at a velocity of 0.1 m/s due to the influence of fluid viscosity. This limitation is alleviated as the box's velocity increases, with a distinct upward displacement of the free surface within the lock being observed, followed by persistent oscillations at an elevated level. Unfortunately, the anticipated simultaneous downward displacement of the free surface remains absent in the experimental results. This absence is likely attributable to the limited space between the box and the lock walls, which restricts the fluid's ability to flow outward from the lock on both sides. It is anticipated that further increases in velocity would mitigate this constraint. Therefore, the model experiment conducted at a velocity of 0.3 m/s has been specifically chosen as a focal point for our case study. This deliberate selection is due to the fact that at this particular velocity, the elevation of the free surface within the lock becomes more prominent.

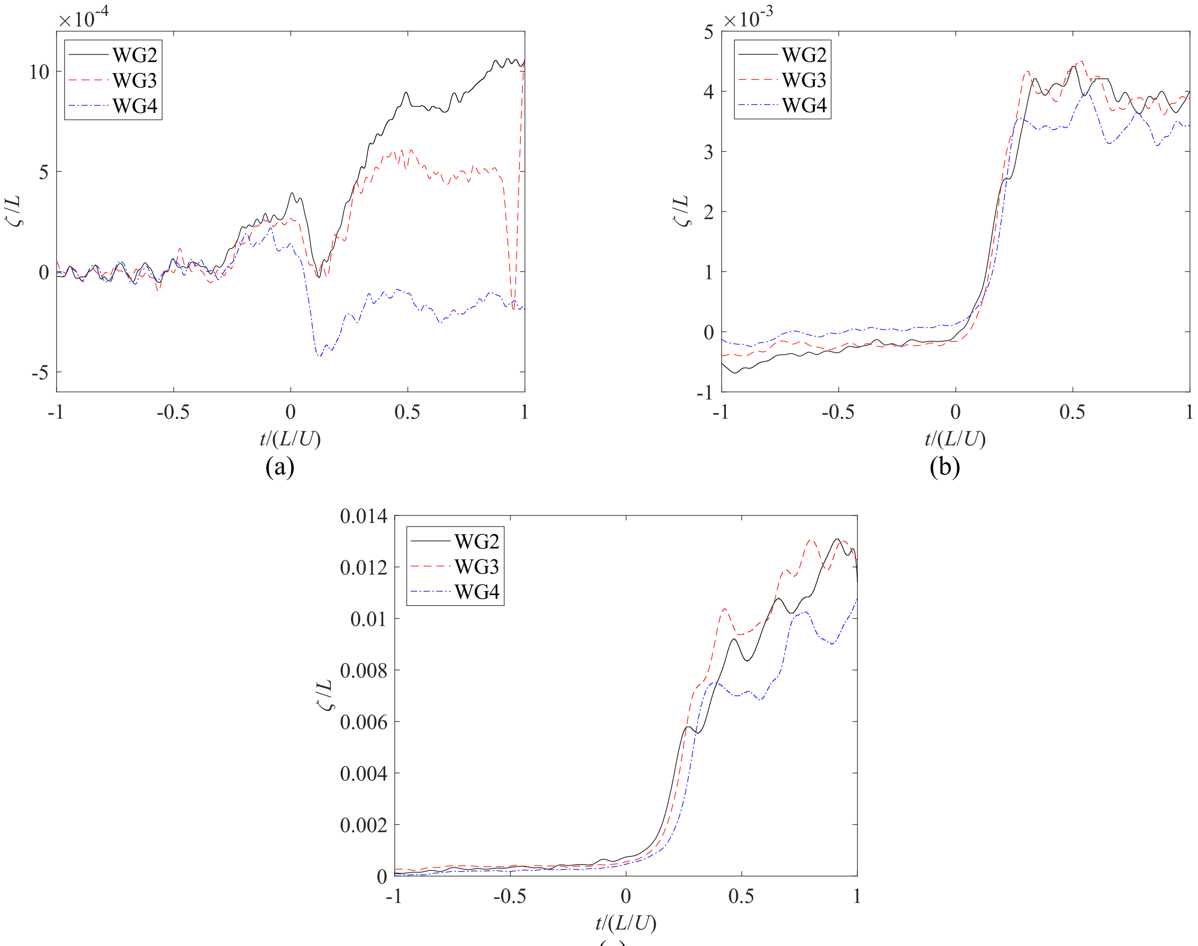

(a)

(b)

(c)

Figure 8 Wave elevations in the lock at different Froude numbers: (a) *Fr* = 0.002; (b) *Fr* = 0.004; and (c) *Fr* = 0.006.

3.2 (a) Validation of the numerical simulation

Firstly, a preliminary validation of the simulation results will be conducted in this section. The model experiment with a velocity of 0.3 m/s has been selected as a case study, not only because at this velocity, the elevation of the free surface inside the lock is more pronounced, but also because the data from this set of experiments has been validated through five repeated trials, as shown Figure 9.

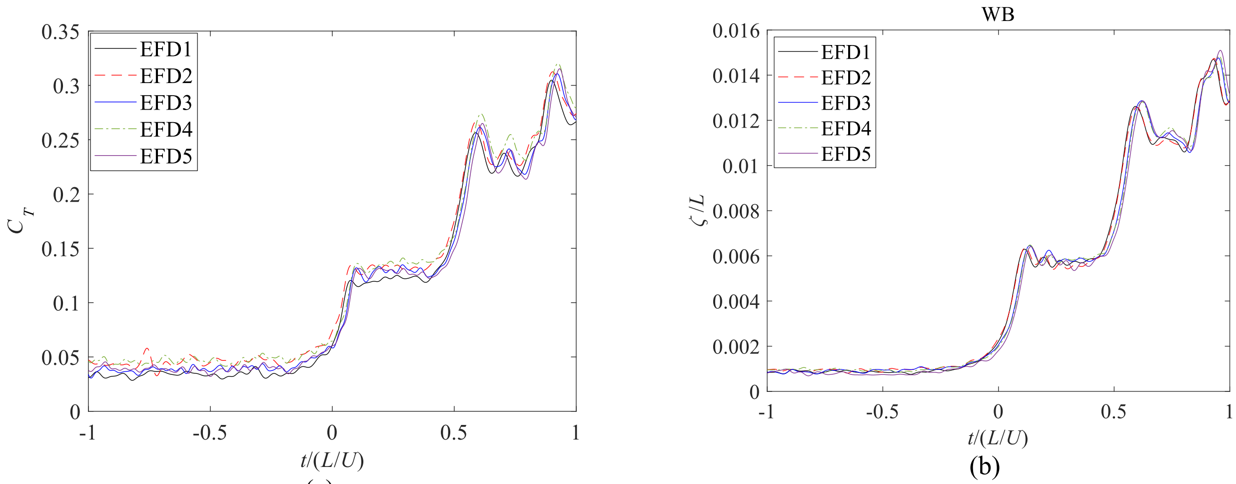

(a)

(b)

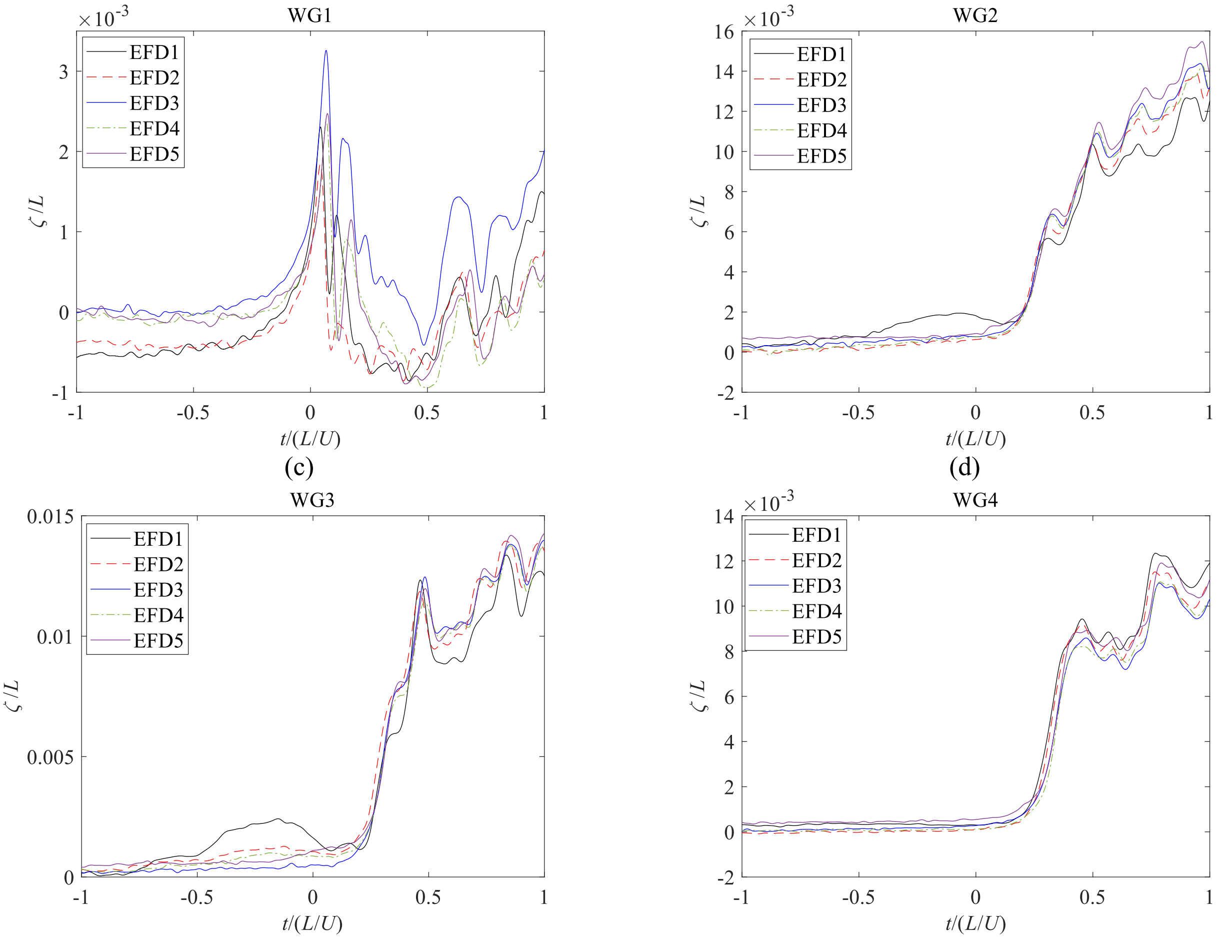

(c) (d)

(e) (f)

Figure 9 Repetitions of the Model Experiment when *U* = 0.3 m/s.

After verifying the accuracy of the experimental results, this paper began to test the simulation results. Figure 10 (a) demonstrates that MHydro effectively predicts the general trend of surge force variation as the box enters the lock, though some finer details are missing. At the initial stage, discrepancies between MHydro and experimental results are evident. These differences stem from MHydro accounting only for wave-making resistance during the box's forward motion, whereas the experimental data reflect total resistance, including frictional forces. With a low Froude number ($Fr = 0.06$) indicative of a very low velocity, frictional resistance becomes a dominant factor in the total resistance, which MHydro does not fully capture. Further evidence supporting this observation is provided in Figure 10 (b), which shows that MHydro effectively captures the wave elevation at the box's bow during its entry into the lock. The experimental results reveal three distinct steps at $t/(L/U)$ values of 0.2, 0.5, and 0.75. The numerical simulation similarly reflects this trend, albeit with slight variations in the step positions.

Figure 11 presents the wave field within the lock during the box's entry. It is evident that the elevation of the bow waves undergoes three distinct transitions, occurring at approximately $t/(L/U)$ values of 0.1, 0.6, and 0.9.

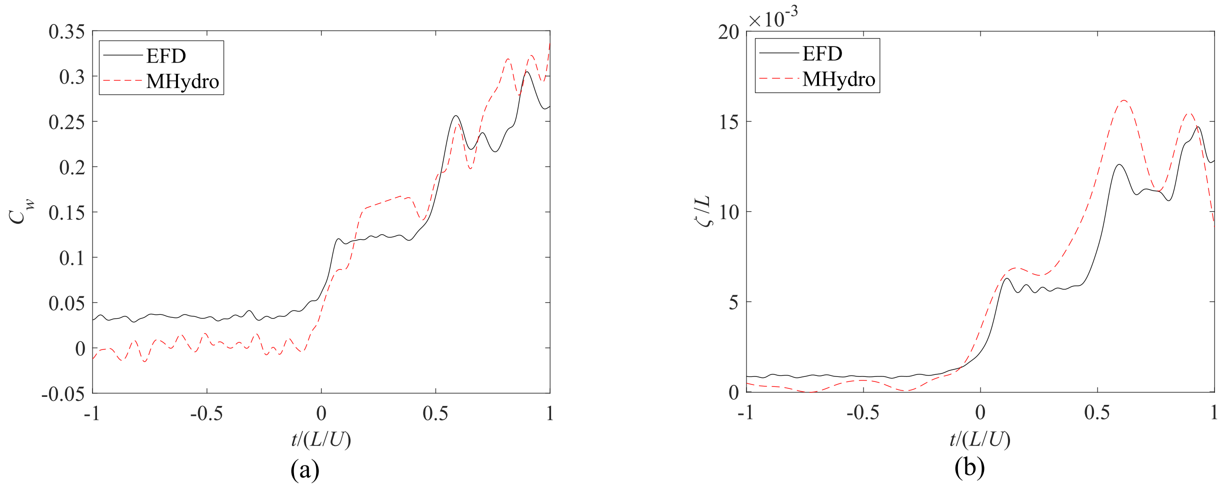

(a) (b)

Figure 10 Comparison of the surge force applied on the box and the wave elevation at the bow while *Fr* = 0.06 where the result from EFD is the total resistance and MHydro's result is wave making resistance: (a) surge force and (b) waves at the bow.

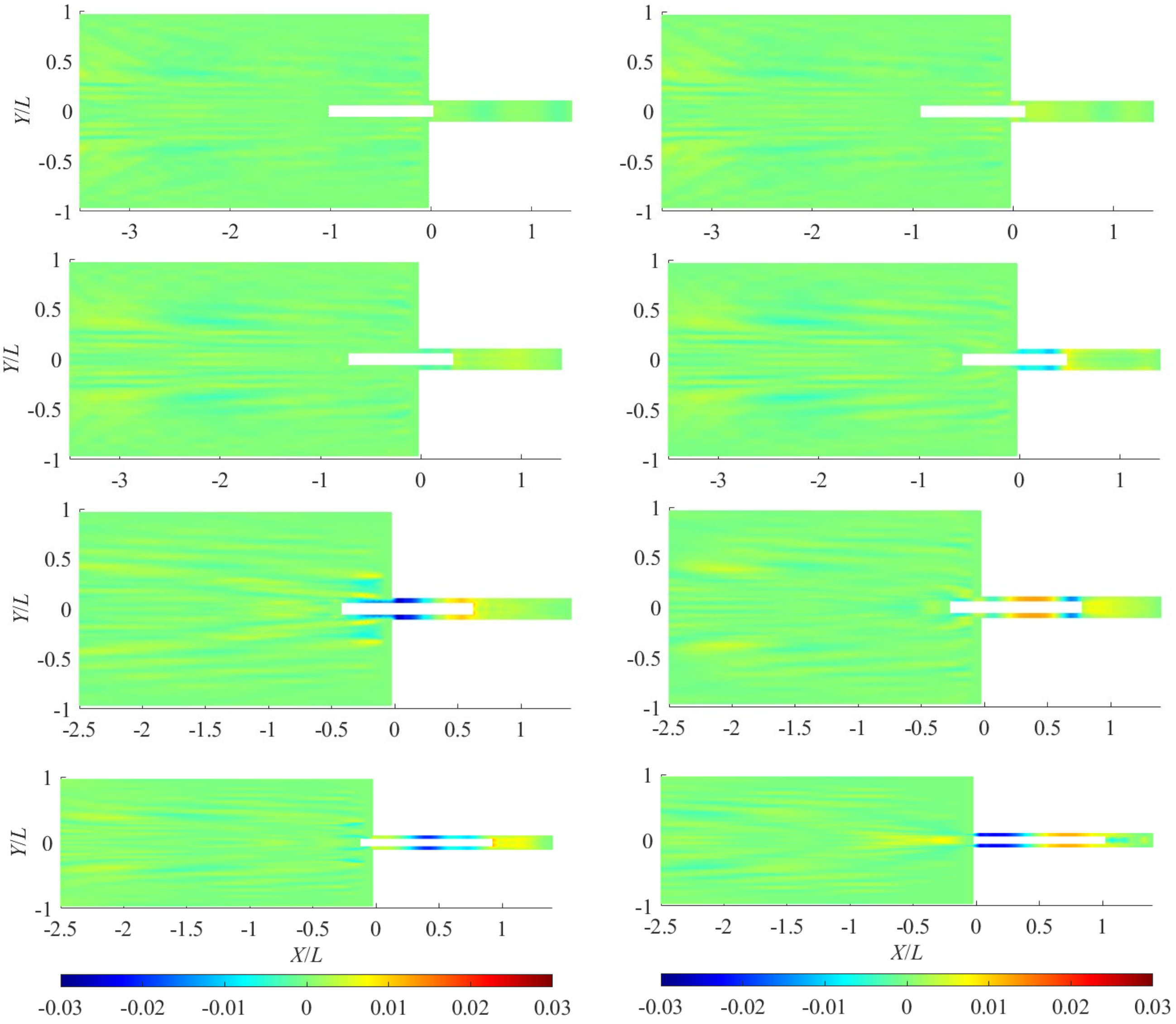

Figure 11 The wave field in the lock when the box is entering the lock, where the color bar represents *ζ/L*

Figure 12 validates the predicted wave heights within the lock, with wave gauge locations shown in Figure 12 (e). The MHydro simulation results generally align well with the experimental fluid dynamics (EFD) data. The wave elevation oscillations are well captured, although some finer details are not fully represented. In contrast, the computational fluid dynamics (CFD) results exhibit excellent agreement up to $t/(L/U)\leqslant 0.6$. Beyond this point, while the experimental results stabilise, the CFD predictions continue to increase. It can also be observed, initially, as the box begins to enter the lock ($t/(L/U)\leqslant 0.2$), the volume of fluid within the lock changes only slightly, resulting in minimal variation in the free surface. As the box progresses further, its kinetic energy is converted into gravitational potential energy, leading to a rapid rise in the free surface. Theoretically, after reaching the peak level, the gravitational potential energy should be transformed back into kinetic energy, causing fluid to flow out of the lock and a subsequent decrease in the free surface. However, this phenomenon was not observed in this case. At $t/(L/U)=0.45$, the free surface reaches its maximum level and continues to oscillate at that point, indicating that the kinetic energy absorbed and lost by the fluid has reached equilibrium, and the free surface height remains relatively constant.

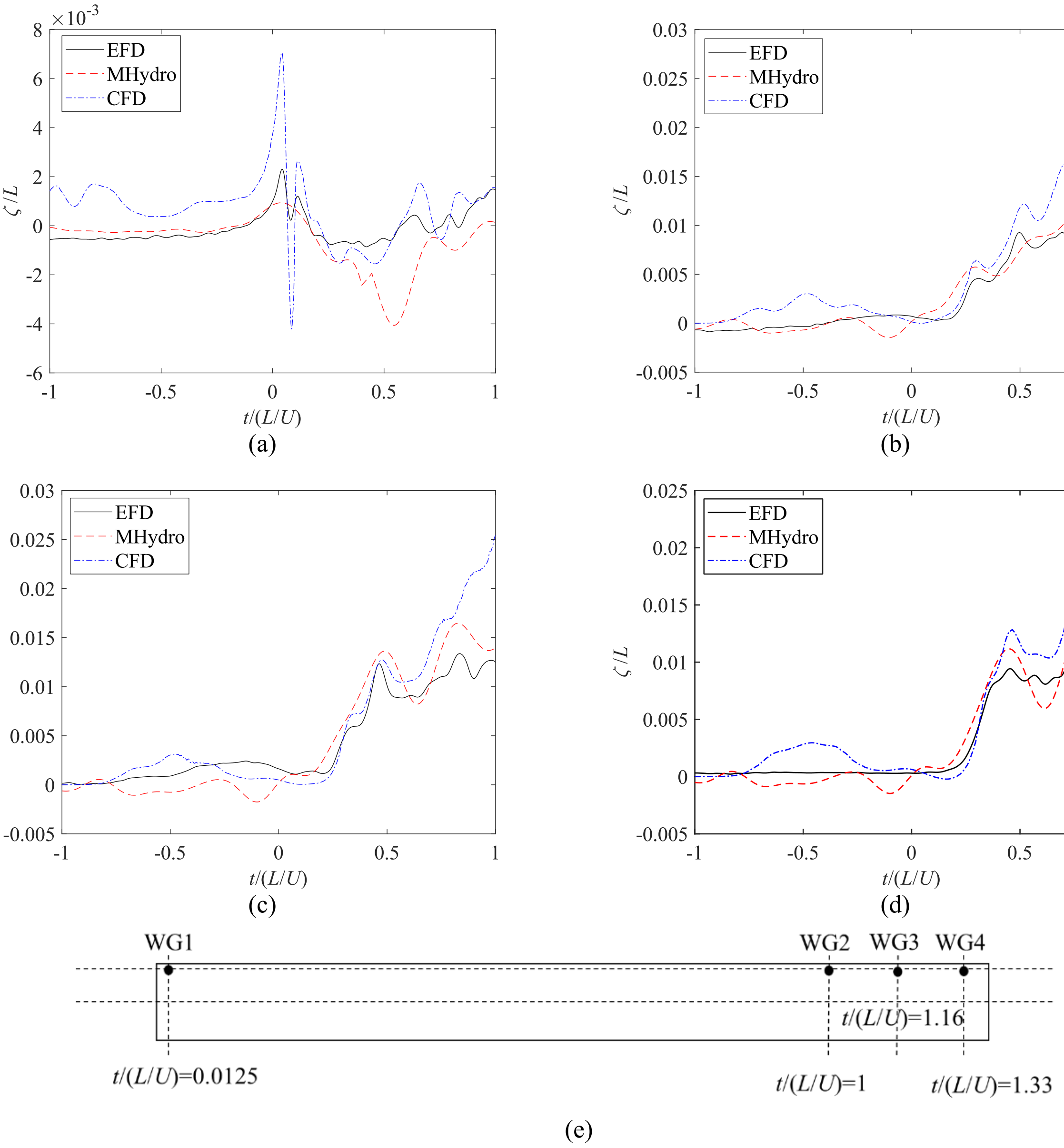

(a) (b) (c) (d) (e)

Figure 12 Comparison of the wave elevations in the lock while *Fr*= 0.06: (a) waves at WG1; (b) waves at WG2; (c) waves at WG3; (d) waves at WG4; and (e) positions of wave gauges.

3.2 (b) Return flow phenomenon

As illustrated in Figure 13, the majority of the hydrodynamic phenomena observed within the lock are predominantly caused by the return flow. When the return flow is excluded from the simulation ($\kappa = 0$), changes in the free surface within the lock are negligible. However, wave resistance is strongly influenced by wave elevations, leading to a significant distortion in the predicted wave-making resistance under such conditions. By comparing simulation outcomes with experimental results, it

was determined that using $\kappa = 15$ produces results that closely match the experimental data. This value represents a balanced compromise, as the coefficient's selection is highly dependent on specific parameters, such as the hull shape.
Furthermore, this study identified that the return flow within the lock is inherently non-uniform. Fluid near the bow of the box is more significantly affected by the return flow compared to areas nearer the lock walls. This discrepancy arises due to the initiation of return flow caused by the box entering the lock. As a result, the flow field surrounding the bow, which moves along with the box, demonstrates a stronger interaction with the return flow than fixed regions farther from the box.

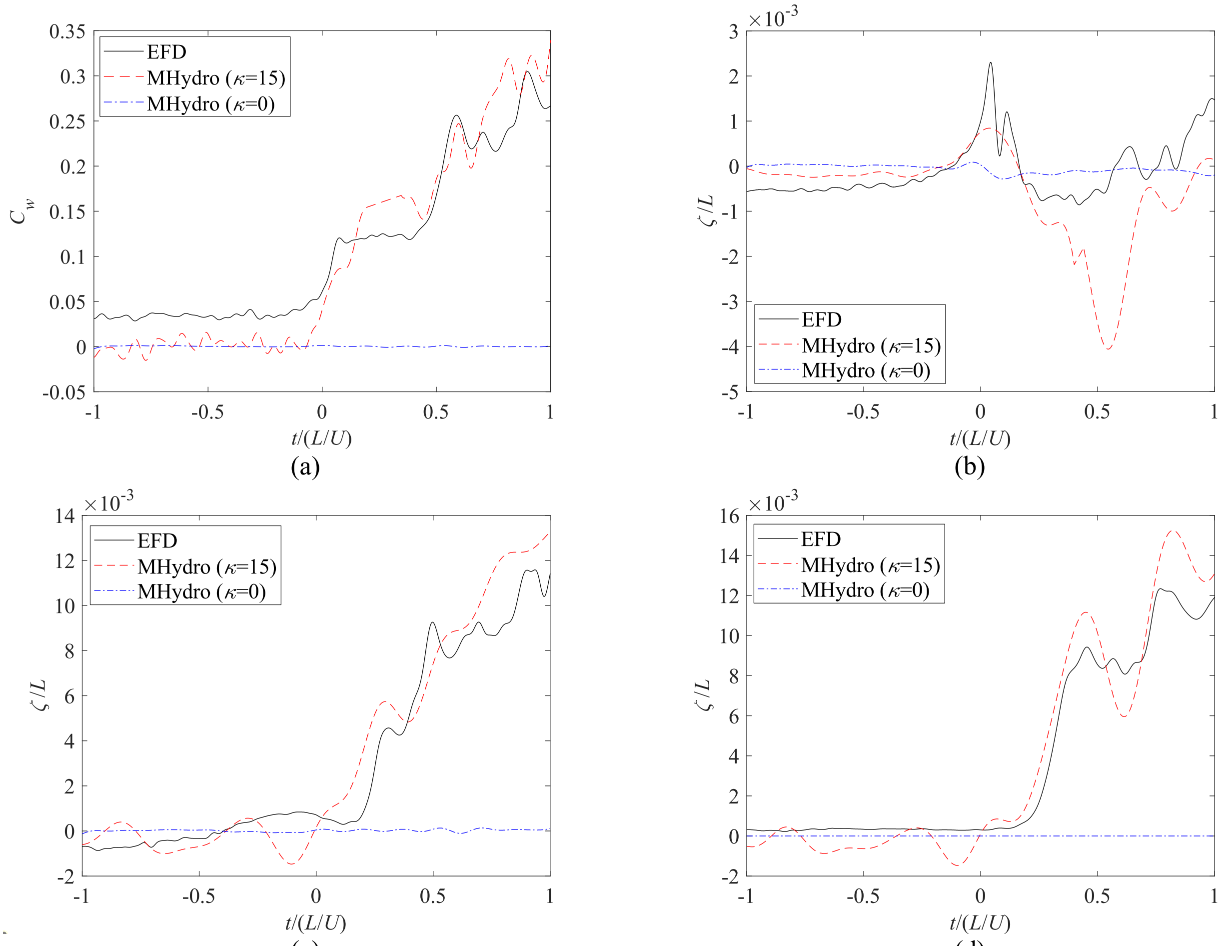

(a) (b)

(c) (d)

Figure 13 Comparison of the numerical simulation results with different acceleration coefficients j while *Fr*=0.06: (a) wave making resistance; (b) waves at WG1; (c) waves at WG2; and (d) waves at WG4.

3.2 (c) Free surface effect and piston phenomenon

Figure 14 compares total resistance and wave-making resistance obtained through different methods. The experimental results from EFD provide the total resistance coefficient C_T, while the MHydro simulations yield only the wave-making resistance coefficient C_w. The numerical simulation results show progressive convergence toward the experimental data as the free surface establishing approach evolves: first treating the free surface as a rigid wall, then introducing a linear quasi-steady free surface, and finally incorporating unsteady effects. Notably, the step phenomena observed in the experimental data are reproduced only when unsteady effects are fully included in the simulations, highlighting their critical role. This explains why the step phenomena become increasingly pronounced with higher box velocities, as greater entry speeds intensify unsteady free surface effects within the lock. Figure 15 further emphasises the importance of employing a 3D free surface model and accounting for its unsteady behaviour to address this problem accurately.
This study also demonstrates that unsteady free surface effects are essential for replicating the piston phenomenon within the lock. If free surface effects are entirely neglected, the water level inside the lock rises sequentially, driven solely by the high-pressure field ahead of the ship's bow. When a linear quasi-steady free surface is incorporated, the water level rises simultaneously across the lock but follows a smooth curve rather than the abrupt elevation observed experimentally. Only the fully unsteady MHydro method successfully reproduces the step-like rise seen in experiments, as depicted in Figure 16.
However, no clear simultaneous decrease in the free surface level was observed in this case. Even so, some trends resembling such behaviour can be identified in the wave profiles at WG3 and WG4. As shown in Figure 16 (a) and Figure 16 (d), during the interval $t/(L/U)$ equals to 0.5 to 0.8, the wave elevations at both locations initially decrease before increasing again, with

the changes occurring simultaneously. This phenomenon arises from the energy dynamics explained earlier and, from an external perspective, is influenced by the larger flow space at these points. Being farther from the lock entrance, these locations allow for a temporary lowering of the free surface.

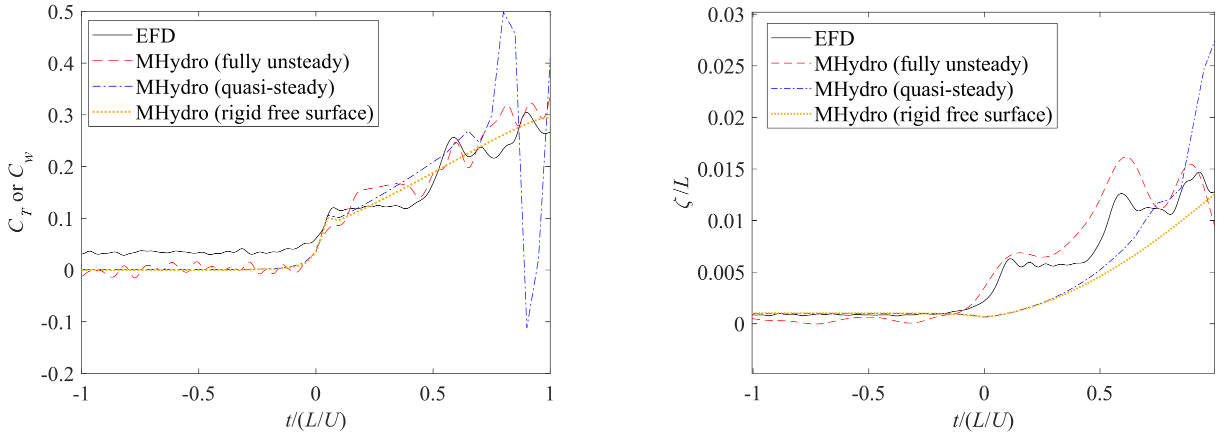

(a) (b)

Figure 14 Resistance applied on the box obtained by different methods: (a) surge force and (b) waves at the bow.

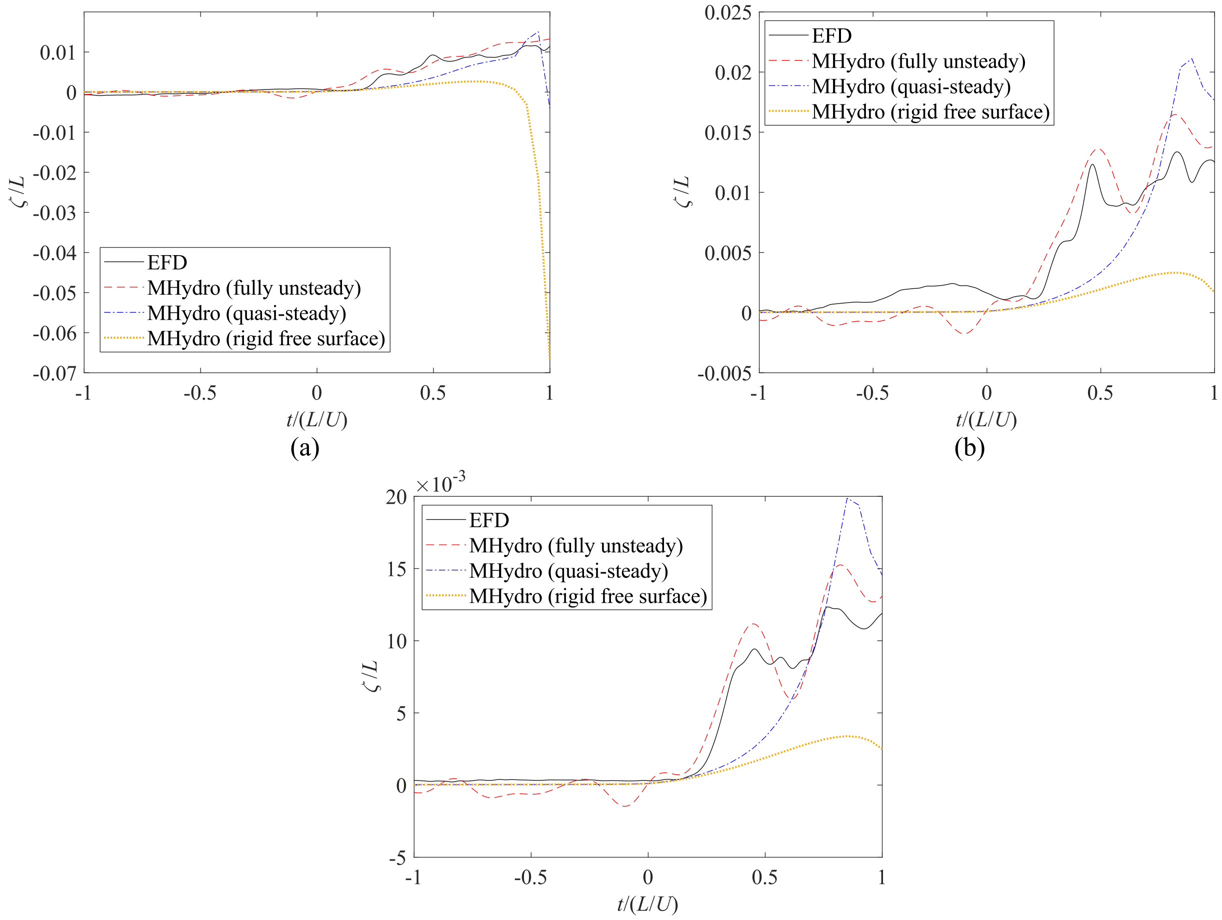

(a) (b)

(c)

Figure 15 Wave elevations inside the lock: (a) waves at WG2; (b) waves at WG3; and (c) waves at WG4.

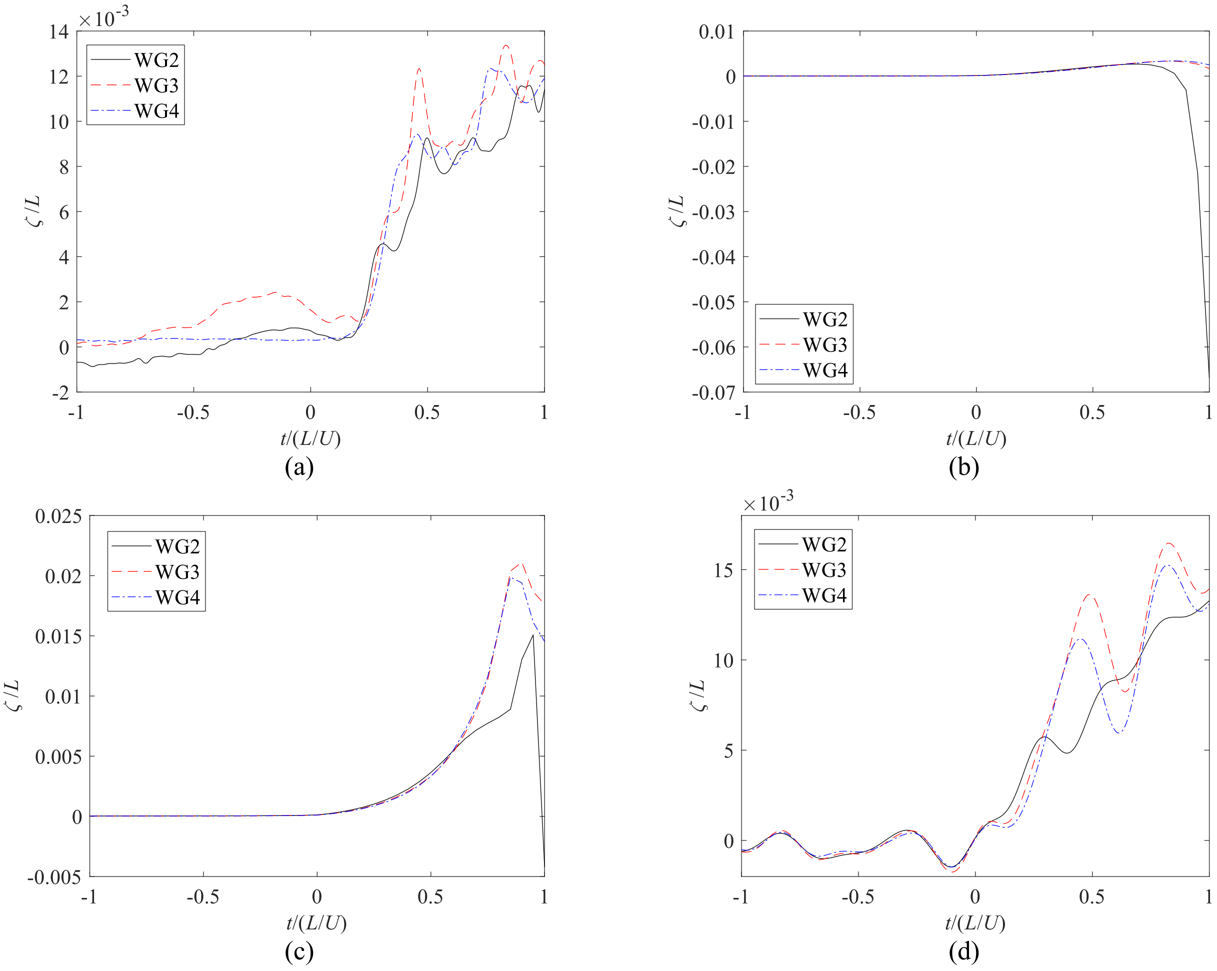

Figure 16 Wave elevations at WG2, WG3, and WG4: (a) EFD results; (b) results with a rigid free surface; (c) results with a quasi-steady free surface; and (d) results with a fully unsteady free surface.

4 CONCLUSION

Through the simulation and analysis of a box entering a lock at low speeds, this study demonstrates that the potential flow solver MHydro effectively captures the forces acting on the box and the general trends of wave generation during lock entry. Nevertheless, it recognises certain limitations in fully resolving the complexities of flow dynamics, attributing these issues to the simplifications inherent in the return flow model employed. The non-uniform distribution of return flow within the lock contributes to inaccuracies in the simulation results, highlighting the need for future advancements in predictive modelling. Furthermore, while a significant piston effect was not observed during the box's entry into the lock—primarily due to the constrained clearance between the box, lock walls, and lock bottom—the study underlines that its absence in this scenario does not preclude its occurrence in other ship-lock interactions. The presence and intensity of the piston effect are strongly influenced by factors such as the ratio of the ship's cross-sectional area to that of the lock and the entry velocity, necessitating further investigation to thoroughly understand its role and implications.

5 REFERENCE

Delefortrie, G., Willems, M., Vantorre, M. & Laforce, E., 2009. *Behavior of post panamax vessels in the third set of panama locks.*

Lataire, E., Delefortrie, G. & Vantorre, M., 2016. *Impact of banks on ship squat.*

Lataire, E., Vantorre, M. & Delefortrie, G., 2009. *Captive model testing for ship to ship operations.*

Lataire, E., Vantorre, M. & Delefortrie, G., 2012. A prediction method for squat in restricted and unrestricted rectangular fairways. Volume 55, pp. 71-80.

Lataire, E., Vantorre, M., Delefortrie, G. & Candries, M., 2012. Mathematical modelling of forces acting on ships during lightering operations. *Ocean Engineering,* Volume 55, pp. 101-115.

Li, M., Yuan, Z. M. & Yeung, R. W., 2020. *Unsteady wave-making resistance of an accelerating ship.*

Liu, Y. et al., 2024. Unsteady hydrodynamics of a surface piercing and fully submerged body when entering a lock. *Physics of Fluids*, 36(6).

Meng, Q. & Wan, D., 2016. URANS simulations of complex flows around a ship entering a lock with different speeds. *International Journal of Offshore and Polar Engineering,* 26(2), pp. 161-168.

Norrbin, N. H., 1976. *Bank effects on a ship moving through a short dredged channel.*

Schoenherr, K., 1960. *Data for estimating bank suction effects in restricted water and on merchant ship hulls.*

Terziev, M., Liu, Y., Yuan, Z. M. & Incecik, A., 2024. The resistance of a trans-critically accelerating ship in shallow water. *Ship Technology Research,* 71(1), pp. 14-32.

Vantorre, M., Verzhbitskaya, E. & Laforce, E., 2002. Model test based formulations of ship-ship interaction forces. *Ship Technology Research,* Volume 49, pp. 124-141.

Vrijburcht, A., 1988. *Calculations of wave height and ship speed when entering a lock,* Report No. PUB-391.

Wan, Z. et al., 2022. Effect of ship-lock induced surges on navigation safety in a branched lower approach channel system. *Journal of Hydrodynamics,* 24(2), pp. 481-496.

Yuan, Z. M., 2019. Ship hydrodynamics in confined waterways. *Journal of Ship Research,* 63(1), pp. 16-29.

6 AUTHORS BIOGRAPHY

Yihan Liu holds the current position of surveyor at China Classification Society. He is responsible for ship inspection, classification and certification. His previous experience includes study unsteady hydrodynamics as a PhD student in University of Strathclyde.

Momchil Terziev is currently a lecturer/assistant professor at the University of Strathclyde. He specialises in Computational Fluid Dynamics modelling for shallow water ship hydrodynamics and scale effects.

Zhi-Ming Yuan holds the current position of Reader at the University of Strathclyde, UK. His research activity is mainly focused on the Marine Hydrodynamics and Offshore Renewable Energy. He has been a member of the 29th-31st ITTC Manoeuvring Committee. Member of the organization and scientific committees of MASHCON conferences since 2022.